Journal of Mines, Metals and Fuels, *73(11): 3523-3541; 2025. DOI: 10.18311/jmmf/2025/49720*

Online ISSN : 0022-2755

Journal of Mines, Metals and Fuels

Contents available at: *www.informaticsjournals.co.in/index.php/jmmf*

Statistical Study of Hybrid Nanofluid Heat Transfer in Porous Rotating Cone

G. B. Pavithra[1,2], R. Sharma[2], V. Nagaradhika[3]* and S. Manjunatha[3]

[1]Government First Grade College, Gundlupete - 571111, Karnataka, India
[2]Department of Mathematics, GSS, GITAM Deemed to be University, Bengaluru - 561203, Karnataka, India
[3]Department of Mathematics, Sir M Visvesvaraya Institute of Technology, Bengaluru - 562157, Karnataka, India; nagaradhika79@gmail.com

Abstract

A numerical study of the flow of a hybrid nanofluid across a vertical cone in motion is detailed in this work. The primary objective of this research is to analyse the processes of heat transfer in the presence of thermal radiation, Darcy-Forchheimer effects, a heat source or sink, a porous medium, a magnetic field, a thermal Grashof number, and slip effects. As a result of the similarity transformation converts partial differential equations into first-order ordinary differential equations. The resultant dimensionless equations are solved using the shooting approach and the open-source program MATLAB (bvp4c). The impacts of key factors are analysed using graphs and tables. While considering sensitivity, the response surface approach examines the outcomes, such as skin friction on the x and y axes and the Nusselt number. R^2 values for all output responses approached 1.0, demonstrating outstanding prediction accuracy for the statistical model. The observed pattern indicates that the magnetic field, the Darcy-Forchheimer effect, and the porous medium reduce the boundary layer thickness. Energy rises with increasing thermal radiation and heat generation parameters, but falls with increasing heat sink and thermal slip impact.

Major Findings: *Plastics, metals, heat transfer, thin coatings, drying goods, medical applications, and nonlinear stretching sheets all make use of these materials to improve process efficiency and product quality.*

Keywords: *Hybrid Nanofluid, Heat Source/Sink, Slip Effects, Thermal Buoyancy, Thermal Radiation*

1.0 Introduction

This investigation is centred on improving the heating rate and current density (magnetic flux) of an electrically conducting fluid that is moving through a vertical porous cone. The effects of an induced magnetic field, thermal radiation, viscous dissipation, and thermal slip are considered. Induced magnetic fields are essential for thermal regulation and the management of sauna-like environments. Heat exchangers, transformers, electrical machines, nuclear research, plasma studies, space uses, and thermonuclear fusion systems are some examples of how thermally driven Magneto-Hydro-Dynamic (MHD) flows along vertical cones are used in modern thermal engineering and industry. Applications for thermal radiation in MHD fluids include gas turbines, food processing, bio-convective flows, energy transport systems, and thermal power production. In addition, thermal radiation plays a crucial role in many fields, including agricultural thermal regulation, polymer heat treatment, geographic systems, and space exploration. Systems include nuclear reactor cooling, high-energy plasma, liquid metals, and power generation also rely heavily on radiative heat transfer. Coating the inside of the cone with a porous material enables both thermoregulation and improved insulation. Using

*Author for correspondence

electromagnetic radiation in fields like geomechanics, soil and rock mechanics, petroleum engineering, reservoir management, filtration systems, batteries, fuel cells, energy-saving technologies, and catalytic processes helps make porous materials better at absorbing heat. With the help of MHD flow models, radiative thermal transfer finds use in a wide variety of applications, including high-temperature resistors, microelectronics, solar thermal devices, refrigeration systems, innovative materials, and thermoelectric equipment[1]. To study the transient heat and mass transport from a vertical cone that is spinning, Chamkha *et al.,*[2] used numerical approaches. Turkyilmazoglu[3] validated earlier results by studying laminar flow across a spinning cone. The stability of the boundary layer was the subject of subsequent investigations[4-6], which investigated whether the instabilities caused by the spinning cone were absolute or convective in character. Incorporating Brownian motion and thermophoresis, the flow of magnetic nanofluids across a spinning cone was investigated in[7]. Raju and Sandeep[8] investigated Casson fluid flow along a cone in relation to the effects of chemical reactions and magnetic field creation. In their work, Towers *et al.,*[9] utilised thorough mean flow modelling to provide similar solutions for compressible fluid flow around several spinning cones in the presence of surface mass flux. Baithalu *et al.,*[10] pointed out that couple stresses and shear rate are important for understanding how the flow behaves when they studied magneto-polar hybrid nanofluid flow over a flexible surface.

The improved thermal performance of hybrid nanoparticles, such as Al_2O_3-CuO in base fluids, was investigated by Karthikeyan *et al*[11]. These nanoparticles provide better heat transfer efficiency, which is important for engineering thermal management. The use of hybrid Al_2O_t-SiO_2 nanoparticles in geothermal systems, as demonstrated by Alli and Roohollah[12], greatly improves heat transmission efficiency, particularly in optimised helical heat exchanger designs. The hybrid nanofluids examined by Umar *et al*[13], especially the Cu-Al_2O_3/water mixtures, are better than regular nanofluids for transferring heat and conducting thermal energy, making them valuable in advanced thermal and engineering applications. Enhanced thermal conductivity and heat transfer in stagnation point flows are advantages of the Cu-Al_2O_3/water and CuO-Ag/water solutions studied by Gaber *et al*[14]. These solutions are useful for sophisticated cooling systems and intricate industrial thermal processes. Thermophysical properties are greatly affected by changes in temperature, volume concentration, and type of nanoparticle, as demonstrated by Safir *et al.,*[15] in their study of CuO/deionised water nanofluids, which outperform those based on Al_2O_t in terms of thermal conductivity and stability.

The effects of buoyancy forces, Prandtl numbers, and nonlinear thermal radiation on boundary layers, temperature, and velocity in Mixed-Hollow-Dynamic (MHD) flows through porous media were studied by Jyoti and Kalita[16]. Injection, on the other hand, disturbs the stability of the flow. The heat source/sink effects in multi-layer hydrodynamic cone flow across porous medium create periodic convective motion, which was examined by Asifa *et al*[17]. Porosity, which increases velocity, and heat sources, which decrease temperature and concentration, affect skin friction and heat transfer rates. In their analysis, Prakash *et al.,*[18] found that Casson fluid velocity is increased by magnetic effects and decreased by a greater Prandtl number and Forchheimer terms. Heat transfer performance is greatly improved by thermal radiation and zeta potential, which both reduce temperature. In their study, Shiv *et al.,*[19] examined how hybrid nanofluids move and discovered that in shapes like cones, wedges, and plates, the speed decreases due to magnetic fields, wall temperatures, and thermal relaxation, while the heat transfer increases with higher wall temperatures and thermal relaxation. Gaffar *et al.*,[20] studied the effect of increasing temperature and thermal boundary layer thickness on heat transfer in rotating cone flows of tangent hyperbolic fluids, where axial and tangential velocities decrease with increasing Weissenberg, magnetic, and Forchheimer numbers. In their study, Nagaraja *et al.,*[21] found that velocity increases as the Deborah number rises, while the Forchheimer number and relaxation-retardation ratio fall. The researchers also found that biomass numbers greatly increase temperature, drawing attention to the behaviour of nanofluids modelled after Jeffrey across curved stretching surfaces. In their study, Joseph *et al.,*[22] found that the speed increases as the Deborah number rises, while the Forchheimer number and relaxation-retardation ratio fall. The researchers also found that Biot numbers greatly increase temperature, drawing

attention to the behaviour of nanofluids modelled after Jeffrey across curved stretching surfaces. The effects of thermal buoyancy and magnetic fields on skin friction, velocity, and temperature were investigated by Nazibuddin Ahmed and Masuma Khanam[23]. In free convection flow over porous media, heat sinks and radiation have a substantial impact on temperature. In their study, Riaz *et al.*,[24] found that porous media improved centreline flow but decreased wall flow velocity; thermal slip was greater, but viscous slip was lower. Increasing the Brinkman number enhanced velocity but decreased thermal distribution. Iqbal *et al.*,[25] used the second law of thermodynamics to show that adding a magnetic field to nanofluids significantly improves heat transfer, making energy delivery more efficient in industrial systems. Hybrid nanofluids considerably improve heat transmission compared to conventional nanofluids, according to research by Mishra *et al.*,[26]. Changes in temperature and radiative heat improve heat transfer as the concentration of nanoparticles increases.

So far as the researchers are aware, no one has used the RSM model to study the flow of a hybrid nanofluid via a vertical cone that is both spinning and equipped with magnetic fields; this would provide a heat source/sink. The above literature analysis demonstrates that RSM models have been shown to be quite useful in resolving nonlinear issues. So, the new part of this research is how well the following processes work: thermal radiation, magnetic field, porous media, Darcy-Forchheimer, thermal Grashof number, heat source/sink, and slip effect on a vertical cone. To simplify the system from Partial Differential Equations (PDEs) to Ordinary Differential Equations (ODEs), the appropriate comparable transformations are applied. The shooting technique in the MATLAB bvp4c package is used for numerical evaluation of the resulting equations. To back up the flow and temperature fields, tables and graphs show a range of parameters. Additionally, the study's math model is supported by statistical analysis of the results, like shear stress in the x and y directions and heat transfer rate, using the Response Surface Methodology. Since they are so good at handling heat and fluids, heat exchangers, chemical reactors, solar collectors, nuclear cooling, HVAC systems, filtration, fluidised bed reactors, and combustion chambers are all physical components that make up the study.

1.2 Mathematical Formulation

In a two-dimensional magnetohydrodynamic system, the boundary layer flow is incompressible and shows steady-state laminar behaviour. As seen in Figure 1, it considers the impact of the magnetic field (B) and the slip limitation. In addition, the following are some of the assumptions that are made to explain flow phenomena:

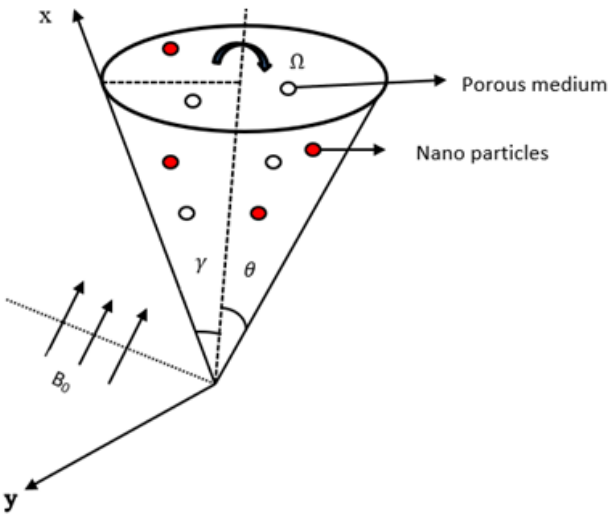


Figure 1. Geometry of the problem.

- The angular velocity is represented by Ω, whereas γ represents the vertex angle of the cone.
- The fluid's temperature is T, the surrounding temperature is T∞, and g is the symbol for gravity.
- ϕ1 and ϕ1 stand for the nanoparticles› solid volume fraction. The fluid›s moving radius, denoted as r, is proportional to x sin γ.
- The components of velocity are u, v, and w in relation to the x, y, and θ directions, respectively.

The basic equations of the Cartesian coordinate system, based on the previous assumption, are:[18,25-27]

$$\frac{u}{r} + u_r + w_y = 0 \tag{1}$$

$$uu_r + vu_y - \frac{w^2}{r} = \frac{\mu_{hnf}}{\rho_{hnf}} u_{yy} + g\beta_t (T - T_\infty) - \frac{\sigma_{hnf} B_0^2}{\rho_{hnf}} u - \frac{\mu_{hnf}}{\rho_{hnf} K_p} u - \frac{C_b}{\sqrt{K_p}} u^2 \quad (2)$$

$$uw_r + vw_y - \frac{uw}{r} = \frac{\mu_{hnf}}{\rho_{hnf}} w_{yy} + g\beta_t (T - T_\infty) - \frac{\sigma_{hnf} B_0^2}{\rho_{hnf}} u - \frac{\mu_{hnf}}{\rho_{hnf} K_p} w - \frac{C_b}{\sqrt{K_p}} w^2 \quad (3)$$

$$uT_r + vT_y = \frac{k_{hnf}}{(\rho C_p)_{hnf}} T_{yy} - \frac{1}{(\rho C_p)_{hnf}} (q_r)_y + \frac{Q_0}{(\rho C_p)_{hnf}} (T - T_\infty) \quad (4)$$

The surface constraints are:[27]

$$u = N_1 \left(\frac{\mu_{hnf}}{\rho_{hnf}} \right) u_y,\ v = 0,\ w = r\Omega,\ T = T_w + D_1 T_y \text{ at } y = 0$$

$$u = 0,\ v = 0,\ T = T_\infty \text{ as } y \to \infty \quad (5)$$

The similarity transformations are as follows:

$$\text{üüßßßß} \quad \sin\gamma \quad '(\eta), \qquad (\nu_f \quad \sin\gamma)^{\frac{1}{2}},$$

$$, \qquad \sin\gamma \quad (\eta)\ \theta(\eta) = \frac{T - T_\infty}{T_w - T_\infty},$$

$$where\ T_w - T_\infty = (T_0 - T_\infty)\frac{r}{L},\ \eta = y\left(\frac{\Omega \sin\gamma}{\nu_f} \right)^{\frac{1}{2}} \quad (6)$$

Thermophysical characteristics for nanoparticles are[28]

$$\rho_{hnf} = (1-\phi_2)\left[(1-\phi_1)\rho_f + \phi_1\rho_{s1}\right] + \phi_2\rho_{s2},$$

$$\mu_{hnf} = \frac{\mu_f}{(1-\phi_1)^{2.5}(1-\phi_2)^{2.5}},$$

$$\frac{\sigma_{hnf}}{\sigma_{nf}} = \frac{\sigma_{s2} + 2\sigma_{nf} - 2\phi_2(\sigma_{nf} - \sigma_{s2})}{\sigma_{s2} + 2\sigma_{nf} + \phi_2(\sigma_{nf} - \sigma_{s2})}, \frac{\sigma_{nf}}{\sigma_f} = \frac{\sigma_{s1} + 2\sigma_f - 2\phi_1(\sigma_f - \sigma_{s1})}{\sigma_{s1} + 2\sigma_f + \phi_1(\sigma_f - \sigma_{s1})},$$

$$(\rho C_p)_{hnf} = (1-\phi_2)\left[(1-\phi_1)(\rho C_p)_f + \phi_1(\rho C_p)_{s1}\right] + \phi_2(\rho C_p)_{s2},$$

$$(\rho\beta)_{hnf} = (1-\phi_2)\left[(1-\phi_1)(\rho\beta)_f + \phi_1(\rho\beta)_{s1}\right] + \phi_2(\rho\beta)_{s2},$$

$$\frac{k_{hnf}}{k_{nf}} = \frac{k_{s2} + 2k_{nf} - 2\phi_2(k_{nf} - k_{s2})}{k_{s2} + 2k_{nf} + \phi_2(k_{nf} - k_{s2})}, \frac{k_{nf}}{k_f} = \frac{k_{s1} + 2k_f - 2\phi_1(k_f - k_{s1})}{k_{s1} + 2k_f + \phi_1(k_f - k_{s1})}, \quad (7)$$

Table 1. Thermophysical properties of base fluids and nanoparticles[29]

	Base fluid	Ferro particles	
	Water	Al_2O_3	CuO
	997.1	3970	4250
C_p(J/kgK)	4179	765	686.2
k(W/mK)	0.613	40	8.95
σUm^{-2}	0.05	1 x 10^{10}	0.85 x 10^{10}

As a result of the automated satisfaction of Equation (1), Equations (2) through (5) are formed.

$$\frac{A_1}{A_2} f''' + 2Gr\theta - \frac{A_3}{A_2} Mf' - \frac{A_1}{A_2} Kf' - Frf'^2 - \left(0.5f'^2 - ff'' - 2g'^2\right) = 0 \quad (8)$$

$$\frac{A_1}{A_2} g'' \text{ÑÑØØ} \theta \quad \frac{A_3}{A_2} Mg \quad \frac{A_1}{A_2} Kg \quad Frg^2 \quad (f'g \quad fg') \quad 0 \quad (9)$$

$$\frac{1}{A_5}(A_4 + R)\theta'' - \Pr\left(0.5f'\theta - f\theta'\right) + \frac{\Pr}{A_5} Q\theta = 0 \quad (10)$$

The corresponding boundary conditions are

$$f' \to 0,\ g \to 0,\ \theta \to 0\ as\ \eta \to \infty \tag{11}$$

Here, the non-dimensional parameters are,

$$Gr = \frac{g\beta_f \cos\gamma\left(T_0 - T_\infty\right)L^3}{v_f^2},\ \Pr = \frac{}{\mu_f C_p},$$

$$M = \frac{\sigma_f B_0^2}{\rho_f \Omega \sin\gamma},\ K = \frac{\mu_f}{K_p \Omega \sin\gamma},\ Fr = \frac{C_b}{L\sqrt{K_p}},$$

$$Q = \frac{Q_0}{\left(\rho C_P\right)\Omega \sin\gamma},\ R = \frac{16\sigma^* T_\infty^3}{3k^* k},$$

$$\gamma_1 = N_1\sqrt{\nu_f \Omega \sin\gamma},\ \gamma_2 = D_1\sqrt{\frac{\Omega \sin\gamma}{\nu_f}} \tag{12}$$

Consideration of physical quantities, such as the x- and y-direction skin friction coefficient and the local Nusselt, is advantageous from an engineering and practical standpoint[27].

$$Cf = \frac{2\tau}{\rho_f\left(\Omega L \sin\gamma\right)^2}, Nu = \frac{Lq_w}{k_f\left(T_w - T_\infty\right)} + q_r \tag{13}$$

Here, τ Are the wall shear stresses and the surface heat flow q_w, as follows

$$\tau = -\mu_{hnf}\left[u_y\right]_{y=0},\ q_w = -k_{hnf}\left(T_y\right)_{y=0} \tag{14}$$

The subsequent dimensionless variants of these equations are as follows:

$$\text{üüü}_x^{1/2}\ Cf_x = -A_1 f \tag{15}$$

$$\mathrm{Re}_x^{-1/2}\ Nu_x = -\left(A_4 + R\right)\theta'(0) \tag{16}$$

1.3 Numerical Procedure

Equations (8) through (11) describe the governing equations and their accompanying boundary conditions in their dimensionless forms. This system of first-order ordinary differential equations is derived by translating this set of linear ordinary differential equations, as stated by Manjunatha *et al.*,[30] The MATLAB 'bvp4c' solver is employed to numerically resolve these. This analysis takes into account the following assumptions:

$$\begin{aligned} &f(\eta) = \Theta_1, f'(\eta) = \Theta_2,\ f''(\eta) = \Theta_3, f'''(\eta) = \Theta'_3, \\ &g(\eta) = \Theta_4\ \text{üüü}(\eta) = \Theta_5\ \ g\ \ (\eta) = \Theta_5 \\ &\theta(\eta) = \Theta_6, \theta'(\eta) = \Theta_7,\ \theta''(\eta) = \Theta'_7 \end{aligned} \tag{17}$$

Using Eq. (17) in Eqs. (8)-(11), we get

$$\Theta'_3 = -\frac{A_2}{A_1}\left(2Gr\Theta_6 - \frac{A_3}{A_2}M\Theta_2 - \frac{A_1}{A_2}K\Theta_2 - Fr{\Theta_2}^2 - \left(0.5{\Theta_2}^2 - \Theta_1\Theta_3 - 2{\Theta_5}^2\right)\right) \tag{18}$$

$$\Theta'_5 = -\frac{A_2}{A_1}\left(2Gr\Theta_6 - \frac{A_3}{A_2}M\Theta_4 - \frac{A_1}{A_2}K\Theta_4 - Fr{\Theta_4}^2 - \left(\Theta_2\Theta_4 - \Theta_1\Theta_5\right)\right) \tag{19}$$

$$\Theta'_7 = \frac{A_5\left(\Pr\left(0.5\Re_2\Re\cong_6{}_1{}_7\right)\ \frac{\Pr}{A_5}Q_6\right)}{\left(A_4 + R\right)} \tag{20}$$

Table 2. Review of the results at M = K = F_r = γ_1 = γ_2 = Q = ϕ_1 = ϕ_2 = 0 Comparing heat transfer to earlier publications

Gr	Pr	Iqbal *et al.*,[26]	Mishra *et al.*,[27]	Present study
0	10	1.40832	1.40835645	1.40835645
1	10	1.60768	1.60764674	1.60764674
10	10	2.35355	2.35354567	2.35354567

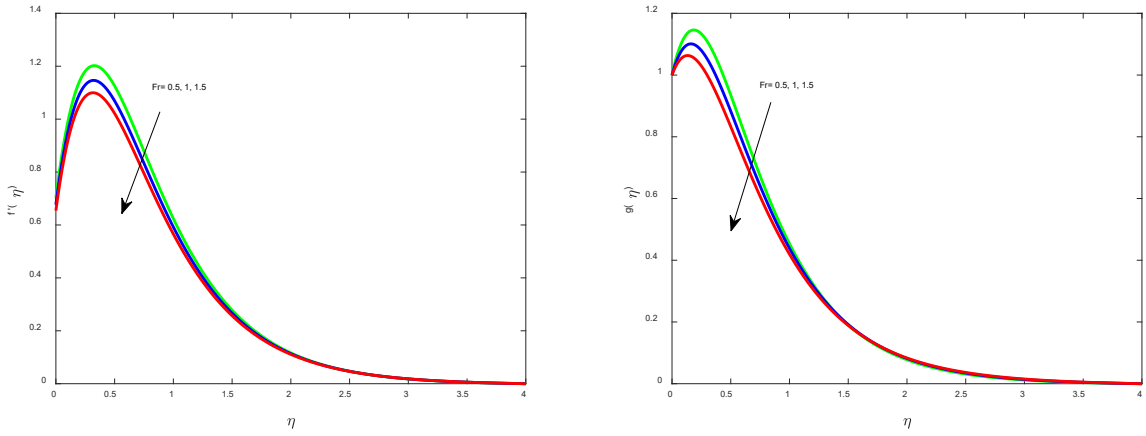
The corresponding boundary conditions are

$$\Theta_2 = \frac{A_1}{A_2}\gamma_1\Theta_3 \text{ üüüü

dimensionless parameters that were defined for numerical computation: M = R = Fr = 0.5, K = Q = $\gamma_1 = \gamma_2$ = 0.2, Gr=10, Pr=6.9.

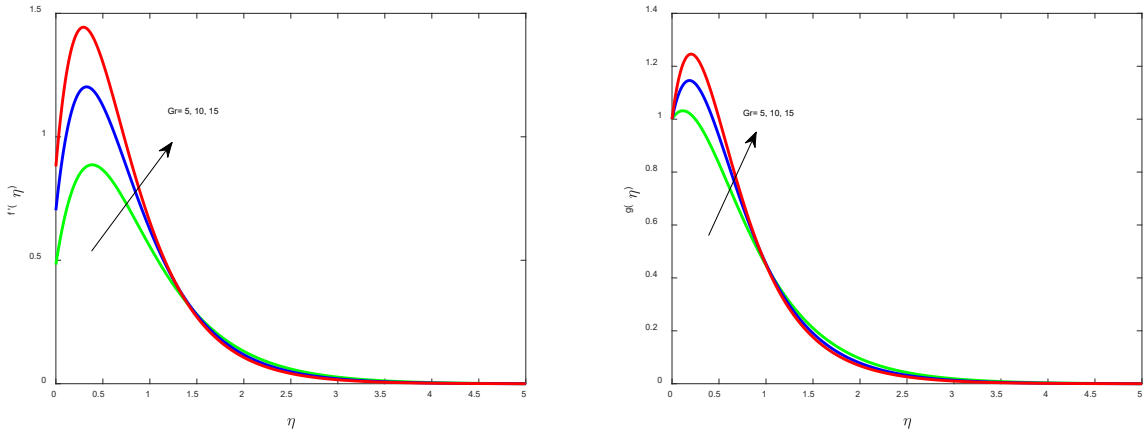
Figure 2 investigates the effect of applying magnetisation characteristics on the fluid's momentum. An interaction between a magnetic field and the motion of charged particles in these fluids causes a Lorentz force to be generated as they flow across the field. Magnetic damping or braking is the result of this force acting counter to the flow of fluid, producing a resistive effect. It slows down the fluid because it reduces its motion. As the magnetic parameter increases, the intensity of this resistive force increases, resulting in a significant decrease in fluid velocity within the boundary layer.

As illustrated by Figure 3, the porosity parameter increases the resistance to flow in a porous material, which in turn affects the momentum of the fluid. In these situations, the solid structure blocks the flow of fluids, and the resistance to flow becomes stronger because higher porosity means lower permeability. The outcome is a discernible slowing of the fluid's velocity due to increased drag or frictional resistance. The interaction between the



(a) (b)

Figure 4. Darcy-Forchheimer effect on **(a)** radial velocity, **(b)** transverse velocity.



(a) (b)

Figure 5. Thermal Grash of number effect on **(a)** radial velocity, **(b)** transverse velocity.

fluid and porous material greatly affects the momentum and overall flow behaviour of non-Newtonian nanofluids moving through porous structures, making this impact particularly noticeable.

Figure 4 examines the effect of the Forchheimer parameter on the velocity field and shows a distinct pattern of a decreasing trend with an increasing parameter. The increased viscosity and inertial forces inside the porous material are responsible for this behaviour. The Forchheimer term considers nonlinear inertial drag, which is more noticeable at higher flow velocities, in addition to the Darcy term, which reflects linear viscous resistance. Non-Newtonian nanofluids in thick porous materials are especially influenced by this effect: as the Forchheimer parameter goes up, the total resistance increases, making it harder for the fluid to move and slowing it down a lot.

The effect of the thermal Grash of number (Gr) on fluid motion is shown in Figure 5, which shows the increasing velocity profiles due to growing thermal buoyancy forces. This value describes the buoyancy strength about the boundary layer viscosity. Buoyancy forces gain dominance as (Gr) grows larger, which boosts velocity and quickens the flow of fluid. Near the surface, the momentum distribution peaks, and as one moves towards the free stream, it steadily decreases. The acceleration of the fluid is due to the intensification of temperature-induced density differences, which cause the fluid to move upwards. Increases in (Gr) result in a more noticeable acceleration of speed.

Figure 6 exhibits the temperature profiles for different values of the thermal radiation parameter (R), showing how the fluid temperature is affected by increasing thermal radiation. Thermal radiation, which makes use of electromagnetic waves (mostly infrared) to transmit heat from warmer to colder objects, raises the temperature of the fluid or surface in question. More energy is transferred to the fluid, increasing its temperature, as the thermal radiation parameter (R) increases. At high temperatures,

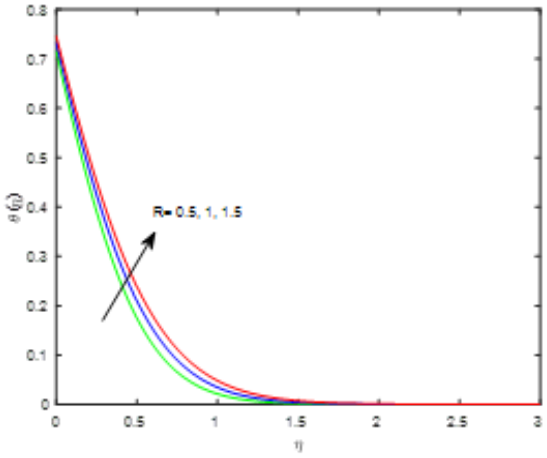
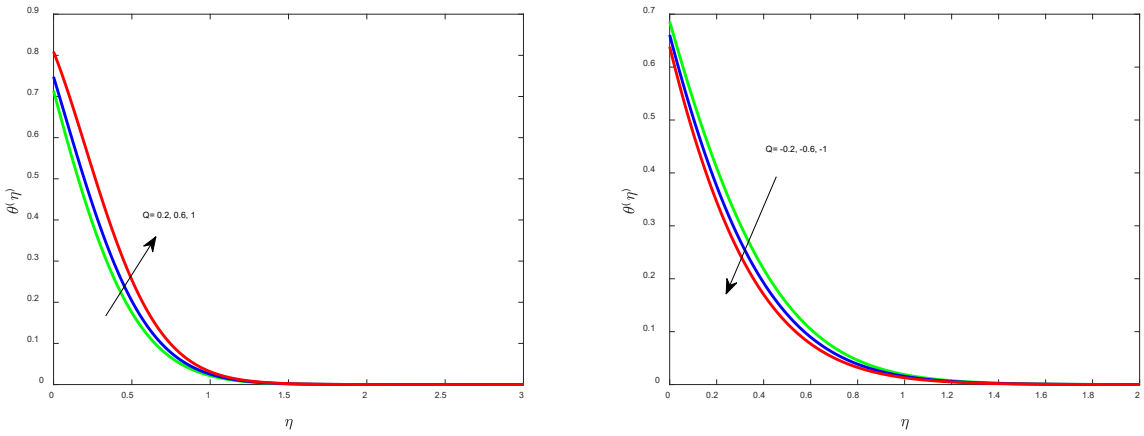
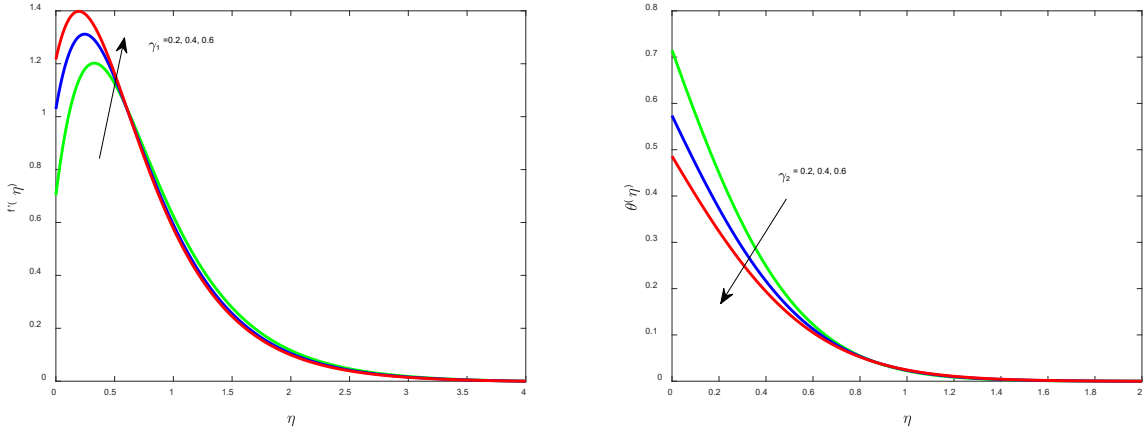


Figure 6. Thermal radiation effect on temperature.



(a) (b)

Figure 7. Effect of temperature on **(a)** heat source and **(b)** heat sink.



(a) (b)

Figure 8. Effect of **(a)** velocity slip on velocity and **(b)** thermal slip on temperature.

this effect becomes much more pronounced because convective movement is supported by a rise in fluid temperature due to radiative heat transfer rather than conduction or convection.

Temperature profiles for various values of the heat source and sink are shown in Figure 7. The higher the heat source, the more thermal energy is delivered to the system, which in turn causes the fluid or surface temperature to rise. The fluid's temperature rises as it absorbs heat from the heat source, which transmits energy to it. On the other hand, as the heat sink draws more heat out of the fluid, the temperature drops. It is possible to lower the temperature of the fluid by using a bigger heat sink, which can absorb more heat. The transmission of heat to the washbasin reduces the system's total energy, resulting in a cooling effect.

The effect of slip velocity on the momentum profile of the fluid is shown in Figure 8(a), which also indicates that variations in the gradient of velocities affect the velocity of the fluid. When no-slip requirements are relaxed, the velocity slip parameter considers the non-zero fluid velocity near the surface, which is the difference between the fluid and wall velocities. Fluid motion is made easier by a decrease in resistance at the fluid-wall contact, which occurs when the velocity slip parameter is raised. Whenever the boundary layer is subject to slip effects, as is the case with rarefied gases or porous media, the total fluid velocity is increased due to this decrease in resistance.

Figure 8(b) demonstrates the way the fluid temperature distribution changes as a function of the thermal slip factor, drawing attention to the impact of the surface temperature gradient. Because there is less thermal resistance at the interface between the fluid and the wall, the fluid's temperature profile increases dramatically as the thermal slip parameter increases. In situations when the temperature gradient is non-zero close to the surface, the thermal slip parameter indicates that there is a temperature differential between the fluid and the wall. In systems where thermal slip happens, like in thin gases or materials with holes, a higher fluid temperature occurs because the reduced resistance to heat transfer allows more heat to move from the wall to the fluid.

2.1 Response surface methodology

An effective method for finding empirical links among various restrictions is the Response Surface Methodology (RSM). This tool is excellent for multi-variable process analysis since it lets you look at inputs that affect the output to different degrees. In this work, RSM is used to examine the effects of several input parameters on skin friction along the x and y axes, as well as on the Nusselt numbers R and Q. These parameters include M, K, and Fr. Tables 3 and 7 show the three levels of testing for each input parameter within given limits[31,32].

Table 2. Impacts of different skin friction parameter settings

Parameter	Symbol	Level		
		-1	0	+1
0.5 ≤ M ≤ 2.5	W_1	0.5	1.5	2.5
0.2 ≤ K ≤ 2.2	W_2	0.2	1.2	2.2
0.5 ≤ Fr ≤ 1.5	W_3	0.5	1	1.5

$$Cf = J_0 + J_1 M + J_2 K + J_3 Fr + J_{11} M^2 + J_{22} K^2 + J_{33} Fr^2 + J_{12} M * K + J_{13} M * Fr + J_{14} K * Fr$$

Table 3. A CCD-based investigative approach

Runs	Coded values			Real values			Response	
	W_1	W_2	W_3	M	K	F_r	Cfx	Cfy
1	-1	-1	-1	2.5	0.2	1.5	3.17283	1.14456
2	1	-1	-1	0.5	0.2	0.5	3.84378	1.89684
3	-1	1	-1	0.5	2.2	1.5	3.17749	1.15096
4	1	1	-1	0.5	2.2	0.5	3.33656	1.40194
5	-1	-1	1	1.5	1.2	1	3.24995	1.27152
6	1	-1	1	1.5	1.2	1	3.24995	1.27152
7	-1	1	1	2.5	0.2	0.5	3.33097	1.39526
8	1	1	1	1.5	1.2	0.5	3.33376	1.3986
9	-1	0	0	2.5	2.2	0.5	3.00565	0.946831
10	1	0	0	1.5	0.2	1	3.45207	1.5139
11	0	-1	0	1.5	1.2	1.5	3.17516	1.14776
12	0	1	0	1.5	1.2	1	3.24995	1.27152
13	0	0	-1	1.5	1.2	1	3.24995	1.27152
14	0	0	1	0.5	0.2	1.5	3.84378	1.89684
15	0	0	0	2.5	1.2	1	3.08181	1.03894
16	0	0	0	1.5	2.2	1	3.08397	1.04208
17	0	0	0	2.5	2.2	1.5	2.89667	0.714827
18	0	0	0	1.5	1.2	1	3.24995	1.27152
19	0	0	0	1.5	1.2	1	3.24995	1.27152
20	0	0	0	0.5	1.2	1	3.45511	1.51729

Tables 4 and 8 demonstrate the generation and execution of the statistical model twenty times after selecting the input parameters. There is a second-order polynomial that models the interaction effects of the input and response variables.

With J0 as the intercept, J1 and J2 as the linear coefficients and the quadratic coefficients, and J3 as the interaction coefficients, the model is constructed using a second-order polynomial. The correlations between the input parameters are captured by the regression coefficients, which modify these terms. To fit the polynomial and measure these connections, the CCD is employed. Six axis points, eight cube points, and six centre points make up this design, which allows for twenty distinct trial runs. Because of its design, factor space exploration is made easier, and regression coefficients are estimated more efficiently.

Data is analysed using an Analysis of Variance (ANOVA), and the findings are displayed in Table 5 to ensure the proposed model is suitable and has practical consequences. Parameters are deemed significant if their p-values are less than 0.05. They are not thought to be important in other places. It is not demonstrated that Fr^2, M*Fr, and K*Fr are relevant. With a score of 98.89%, the

Table 5. Analysis of Variance (ANOVA) of Cfx

Source	Degrees of freedom	Adjusted sum of squares	Adjusted mean squares	F-value	p-value	Co efficient
Model	9	1.03097	0.114552	98.67	0.000	
Linear	3	0.96385	0.321282	276.74	0.000	3.2449
M	1	0.47037	0.470365	405.15	0.000	-0.2169
K	1	0.45928	0.459283	395.61	0.000	-0.2143
Fr	1	0.03420	0.034198	29.46	0.000	-0.0585
Square	3	0.02325	0.007749	6.67	0.009	
M*M	1	0.00268	0.002679	12.31	0.010	0.0312
K*K	1	0.00260	0.002604	8.24	0.005	0.0308
Fr*Fr	1	0.00081	0.000815	0.70	0.422	0.0172
2-Way Interaction	3	0.04387	0.014624	12.60	0.001	
M*K	1	0.04090	0.040902	35.23	0.000	0.0715
M*Fr	1	0.00146	0.001459	1.26	0.288	-0.0135
K*Fr	1	0.00151	0.001510	1.30	0.281	-0.0137
Error	10	0.01161	0.001161			
Lack-of-Fit	5	0.01161	0.002322	*	*	
Pure Error	5	0.00000	0.000000			
Total	19	1.04258				

$$Cfx = 3.2449 - 0.2169M - 0.2143K - 0.0585Fr + 0.0312M^2 + 0.0715M * K$$

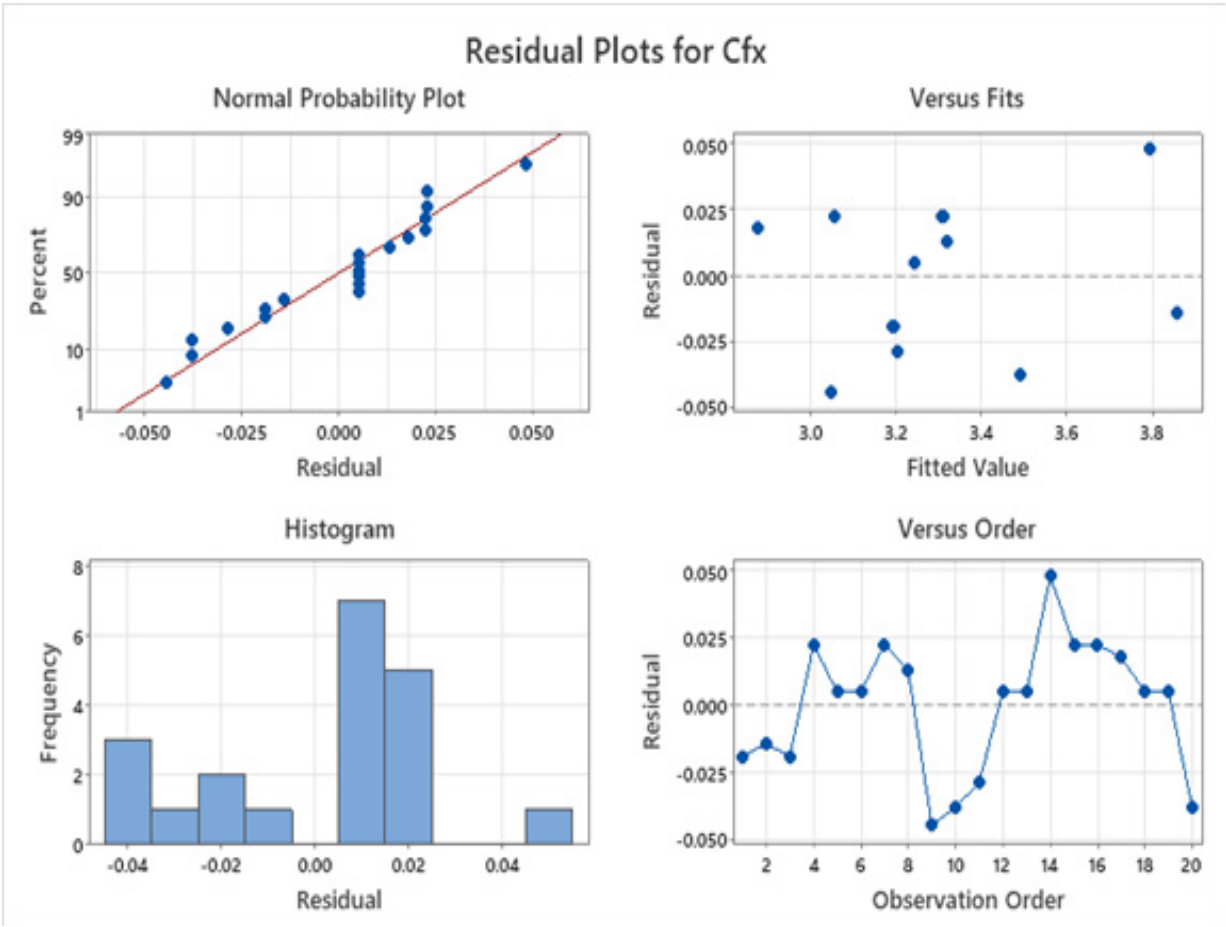


Figure 9. Residual graphs vs. observation for Cfx.

Table 6. Analysis of Variance (ANOVA) of Cfy

Source	Degrees of freedom	Adjusted sum of squares	Adjusted mean squares	F-value	p-value	Co efficient
Model	9	1.49545	0.166161	118.29	0.000	
Linear	3	1.45638	0.485461	345.60	0.000	1.2668
M	1	0.68825	0.688250	489.97	0.000	-0.2623
K	1	0.67120	0.671205	477.84	0.000	-0.2591
Fr	1	0.09693	0.096929	69.00	0.000	-0.0985
Square	3	0.00917	0.003056	2.18	0.154	
M*M	1	0.00092	0.000924	0.66	0.436	0.0183
K*K	1	0.00091	0.000911	0.65	0.439	0.0182
Fr*Fr	1	0.00049	0.000493	0.35	0.567	0.0134

2-Way Interaction	3	0.02989	0.009964	7.09	0.008	
M*K	1	0.01644	0.016436	11.70	0.007	0.0453
M*Fr	1	0.00671	0.006712	8.78	0.004	-0.0290
K*Fr	1	0.00674	0.006744	8.78	0.004	-0.0290
Error	10	0.01405	0.001405			
Lack-of-Fit	5	0.01405	0.002809	*	*	
Pure Error	5	0.00000	0.000000			
Total	19	1.50949				

$$Cfy \cong 1.2668 \quad 0.2623M \quad 0.2591K \quad 0.0985Fr \quad 0.0453M * K \quad 0.290M * Fr \quad 0.290K * Fr$$

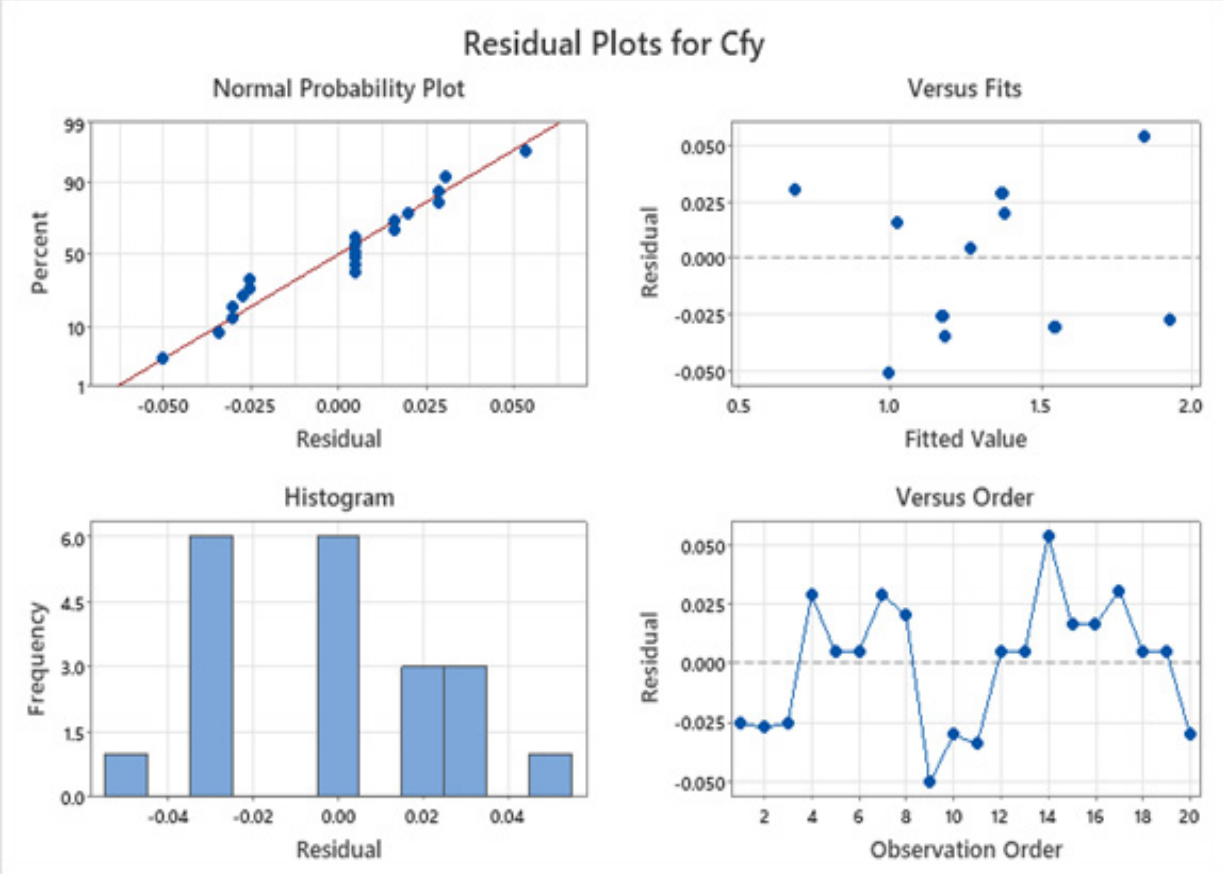


Figure 10. Residual graphs vs. observation for Cfy.

model is clearly accurate. Findings from the data analysis show the following correlation between the x-axis skin friction values and the three input variables: M, K, and Fr.

Table 6 displays the results of an analysis of variance (ANOVA) conducted on the data, which was used to verify that the proposed model is suitable and has practical consequences. A parameter is deemed significant if its

Table 7. Impacts of different Nusselt number parameter settings

Parameter	Symbol	Level		
		-1	0	+1
0.5 ≤ R ≤ 1.5	W_1	0.5	1	1.5
0.2 ≤ Q ≤ 1	W_2	0.2	0.6	1

$$Nu = J_0 + J_1 R + J_2 Q + J_{11} R * R + J_{22} Q * Q + J_{12} R * Q$$

Table 8. A CCD-based investigative approach

Runs	Coded values		Real values		Nu
	W_1	W_2		Q	
1	0	1	1.5	0.2	3.44137
2	-1	1	0.5	0.2	2.31449
3	1	1	1	0.6	2.58215
4	1	1	1	0.2	2.89806
5	1	1	0.5	0.6	2.04334
6	-1	1	1.5	1	2.64855
7	0	1	1	0.6	2.58215
8	-1	1	1	0.6	2.58215
9	1	1	1	0.6	2.58215
10	0	1	1.5	0.6	3.0857
11	0	1	1	1	1.5705
12	0	1	1	0.6	2.58215
13	-1	1	0.5	1	1.72735

$$Nu = 2.5385 + 0.5151R - 0.4513Q + 0.135R * R - 0.0514R * Q$$

p-value is less than 0.05. In other places, they aren't given much thought. No significance is demonstrated for M^2, K^2, Fr^2, M*Fr, and K*Fr. The score of 99.07% demonstrates the precision of the model. This is the result of looking at the data: the y-axis skin friction values are related to the input values (M, K, and Fr).

Table 9 provides the results of the ANOVA study, which support the model's relevance and practical applicability. When the p-value is less than 0.05, the parameter is deemed to have statistical significance. It appears to me that Q*Q is not statistically significant. With an R-value of 99.50%, the model is quite accurate. According to the

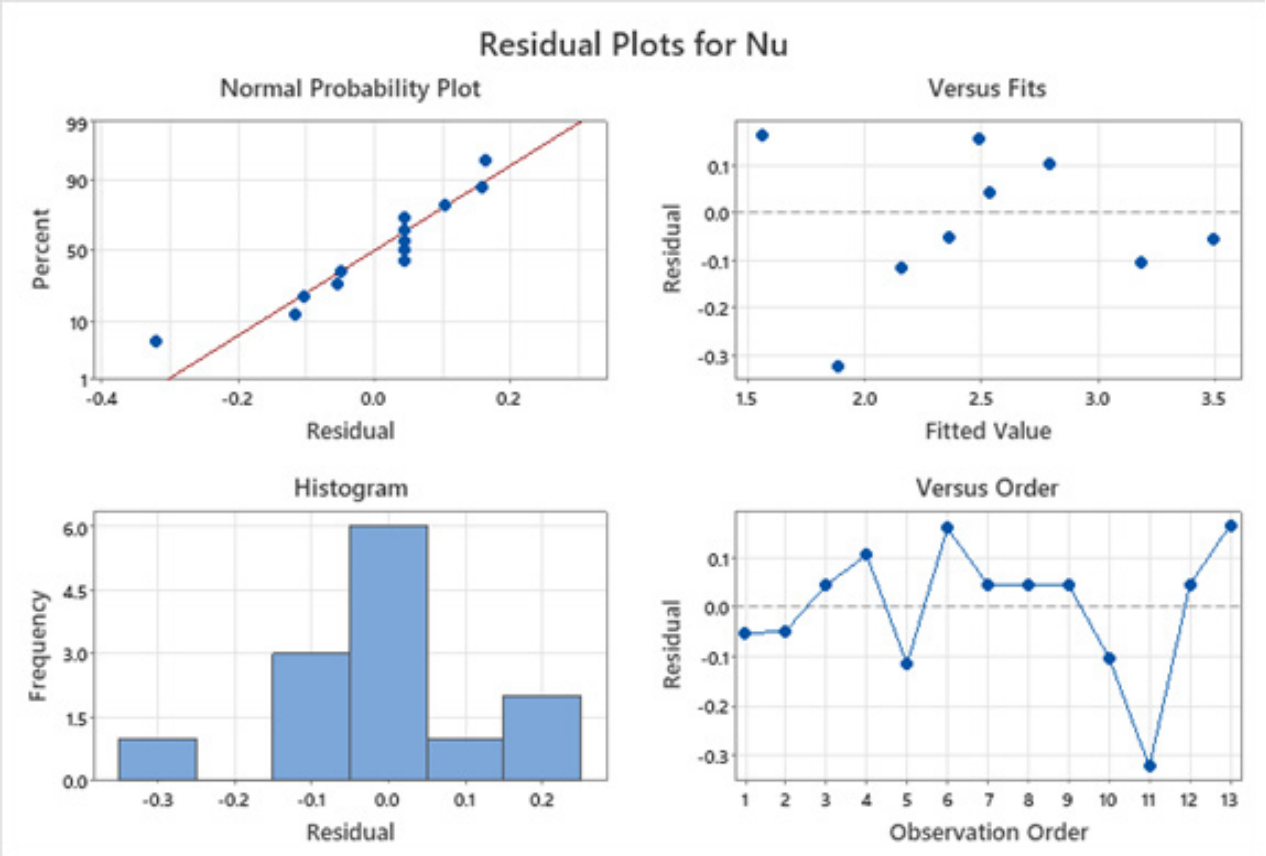


Figure 11. Residual graphs vs. observation for Nu

Table 9. Analysis of Variance (ANOVA) of Nu

Source	Degrees of freedom	Adjusted sum of squares	Adjusted mean squares	F-value	p-value	Co efficient
Model	5	2.94128	0.58826	20.13	0.001	
Linear	2	2.81358	1.40679	48.13	0.000	2.5385
R	1	1.59180	1.59180	54.46	0.000	0.5151
Q	1	1.22178	1.22178	41.80	0.000	-0.4513
Square	2	0.11712	0.05856	2.00	0.205	
R*R	1	0.05038	0.05038	9.72	0.031	0.135
Q*Q	1	0.10521	0.10521	3.60	0.100	-0.195
2-Way Interaction	1	0.01058	0.01058	0.36	0.566	
R*Q	1	0.01058	0.01058	7.36	0.006	-0.0514

Error	7	0.20461	0.02923			
Lack-of-Fit	3	0.20461	0.06820	*	*	
Pure Error	4	0.00000	0.00000			
Total	12	3.14588				

results, there is a connection between the input values (R and Q) and the Nusselt number in the analysis.

Figures 9, 10, and 11 show the study's residual plots for the x-axis skin friction, the y-axis skin friction, and the Nusselt number. Regression probability mapping's positive condition demonstrates that the residuals follow a normal distribution. It is also possible to observe a normal distribution in the residual histogram. A good arrangement has been made for the biggest scraps. Still, looking at the overall trend and residual quality, we can say that the proposed model is helpful and gives a satisfactory match. This study's quadratic model accurately represents the variability in the response variables: Nusselt number, skin friction on the x-axis, and skin friction on the y-axis.

3.0 Conclusions

A non-Newtonian hybrid nanofluid's flow on a vertical cone in motion is the subject of this investigation. Permeable media, according to Darcy's Law, allow the flow to take place. The study considers a variety of factors, including thermal radiation, heat source/sink, magnetic field, Darcy-Forchheimer effect, thermal Grashof number, and so on. To acquire numerical answers for the model, the shooting method and the BVP4C package were utilised. They display these results graphically and tabulatively, drawing attention to important aspects of heat transfer and flow. The researchers further analysed the data using the response surface technique to comprehensively understand the flow dynamics and thermal properties. Here is a rundown of the most important points made by the researchers.

- The porous parameter, magnetic parameter, and Darcy-Forchheimer parameter all result in reduced swirl and radial velocity profiles. The thermal Grashof numbers and velocity slip, on the other hand, demonstrated the exact opposite trend.
- While heat sources and thermal radiation both raise temperatures, heat sinks and thermal slip effects show the reverse tendency.
- Nusselt number models, skin friction in swirl and radial directions, and both have R^2 values of 99.50%, 99.07%, and 98.89%, respectively.
- The scope of this work may be expanded to include various non-Newtonian and Newtonian models, combinations of nanoparticles, and approaches to studying the mathematical model in relation to various physical conditions.

3.1 Future work

- Nanofluid flows across a cone sheet with varying boundary conditions.
- Williamson (or) Carrie nanofluids flow on exponential, linear, cylindrical, and wedge stretching surfaces, exhibiting nonlinear thermal radiation effects.

4.0 References

1. Alqahtani B, El-Zahar ER, Riaz MB, Seddek LF, Ilyas A, Ullah Z, Akgül A. Computational analysis of microgravity and viscous dissipation impact on periodical heat transfer of MHD fluid along porous radiative surface with thermal slip effects. Case Stud Therm Eng. 2024; 60:104641. https://doi.org/10.1016/j.csite.2024.104641
2. Chamkha AJ, Al-Mudhaf A. Unsteady heat and mass transfer from a rotating vertical cone with a magnetic field and heat generation or absorption effects. Int J Therm Sci. 2005; 44(3):267-76. https://doi.org/10.1016/j.ijthermalsci.2004.06.005
3. Turkyilmazoglu M. On the purely analytic computation of laminar boundary layer flow over a rotating cone. Int J Eng Sci. 2009; 47(9):875-82. https://doi.org/10.1016/j.ijengsci.2009.05.008

4. Garrett SJ, Hussain Z, Stephen SO. The cross-flow instability of the boundary layer on a rotating cone. J Fluid Mech. 2009; 622:209-32. https://doi.org/10.1017/S0022112008005181
5. Garrett SJ, Hussain Z, Stephen SO. Boundary-layer transition on broad cones rotating in an imposed axial flow. AIAA J. 2010; 48(6):1184-94. https://doi.org/10.2514/1.J050021
6. Garrett SJ, Peake N. The absolute instability of the boundary layer on a rotating cone. Eur J Mech B Fluids. 2007; 26(3):344-53. https://doi.org/10.1016/j.euromechflu.2006.08.002
7. Nadeem S, Saleem S. Theoretical investigation of MHD nanofluid flow over a rotating cone: an optimal solution. Inf Sci Lett. 2014; 3(2):55-62. https://doi.org/10.12785/isl/030203
8. Raju CSK, Sandeep N. Opposing and assisting flow characteristics of radiative Casson fluid due to a cone in the presence of an induced magnetic field. Int J Adv Sci Technol. 2016; 88:43-62. https://doi.org/10.14257/ijast.2016.88.05
9. Towers PD, Garrett SJ. Similarity solutions of compressible flow over a rotating cone with surface suction. Therm Sci. 2016; 20(2):517-28. https://doi.org/10.2298/TSCI130408032T
10. Baithalu R, Mishra SR, Pattnaik PK, Panda S. Optimising shear and couple stress analysis for the magneto-micropolar dissipative nanofluid flow toward an elongating surface: a comprehensive RSM-ANOVA investigation. J Therm Anal Calorim. 2024; 149(4):1697-713. https://doi.org/10.1007/s10973-023-12741-w
11. Karthikeyan S, Ali F, Thamaraikannan N, Loganathan K. Computational analysis of carboxymethyl cellulose water-based Casson hybrid nanofluid (Al_2O_3-CuO) flow past a wedge, cone and plate. Mod Phys Lett B. 2025; 39(12):24504797. https://doi.org/10.1142/S0217984924504797
12. Shariati A, Rafee R. Reducing the length of the conical geothermal heat exchanger by using variable pitch and hybrid nanoparticles of Al_2O_3 and SiO_2. J Therm Anal Calorim. 2025; 150:8369–8387. https://doi.org/10.1007/s10973-024-13980-1
13. Khan U, Adnan, Ullah B, Wahab HA, Ullah I, Almuqrin MA, Khan I. Comparative thermal transport mechanism in Cu-H2O and Cu-Al_2O_3/H_2O nanofluids: numerical investigation. Waves Random Complex Media. 2025; 35(1):482-97. https://doi.org/10.1080/17455030.2021.2023783
14. Gaber A, Mohamed M, Moatimid G. Maxwell hybrid nanofluid (Cu-Al_2O_3/water) and (CuO-Ag/water) near a stagnation point above an extending sheet. Eur J Pure Appl Math. 2025; 18(1):5773. https://doi.org/10.29020/nybg.ejpam.v18i1.5773
15. Safir NH, Razlan ZM, Ramasamy G, Bakar SA, Abdullah MZ. Investigation of thermodynamic properties and stability of metal oxide (CuO and Al_2O_3)/deionized water nanofluids for enhanced heat transfer applications. 2024. https://doi.org/10.21203/rs.3.rs-4006787/v1
16. Dutta BJ, Kalita B. Effects of nonlinear thermal density variation and radiation on MHD mixed convection through a porous medium over a permeable vertical plate: a numerical approach. Heat Transf. 2025; 54(5):3163-3178. https://doi.org/10.1002/htj.23341
17. Ilya A, Ashraf M, Ali A, Shah Z, Kumam P, Thounthong P. Heat source and sink effects on periodic mixed convection flow along the electrically conducting cone inserted in porous medium. PLoS One. 2021; 16(12):0260845. https://doi.org/10.1371/journal.pone.0260845
18. Prakash J, Tripathi D, Kumar Tiwari A, Kumar Pandey A. Melting heat transfer and irreversibility analysis in Darcy-Forchheimer flow of Casson fluid modulated by EMHD over cone and wedge surfaces. Therm Sci Eng Prog. 2024; 52:102680. https://doi.org/10.1016/j.tsep.2024.102680
19. Singh SP, Upreti H, Kumar M. Flow and heat transfer assessment in magnetized Darcy-Forchheimer flow of Casson hybrid nanofluid through cone, wedge, and plate. Bionanoscience. 2024; 14(1):395-408. https://doi.org/10.1007/s12668-023-01253-4
20. Gaffar SA, Bég OA, Kuharat S, Bég TA. Computation of hydromagnetic tangent hyperbolic non-Newtonian flow from a rotating non-isothermal cone to a non-Darcy porous medium with thermal radiative flux. Phys Open. 2024; 19:100216. https://doi.org/10.1016/j.physo.2024.100216
21. Nagaraja B, Gireesha BJ, Soumya DO, Almeida F. Characterisation of MHD convective flow of Jeffrey nanofluid driven by a curved stretching surface by employing Darcy-Forchheimer law of porosity. Waves Random Complex Media. 2025; 35(1):73-92. https://doi.org/10.1080/17455030.2021.2020933
22. Joseph Sademaki L, Prabhakar Reddy B, Matao PM. A numerical simulation of unsteady dissipative MHD Casson nanofluid transport over an inverted cone with variable heat source/consumption and high order of

reacting species. Multiscale Multidiscip Model Exp Des. 2025; 8(5):230. https://doi.org/10.1007/s41939-025-00809-z

23. Khanam M, Ahmed N. MHD nonlinear natural convection from a uniformly moving porous vertical plate with constant heat and mass flux in the presence of thermal radiation, diffusion-thermo, heat sink, and chemical reaction. Heat Transf. 2024; 53(2):867-92. https://doi.org/10.1002/htj.22979
24. Riaz A, Nawaz MD, Aslam MN, Khan SU, Ur Rehman S, Alhamzi G. Effect of boundary slips and magnetohydrodynamics on peristaltic mechanism of Jeffrey nanofluid along with microorganisms through a porous medium. Heliyon. 2024; 10(13):33949. https://doi.org/10.1016/j.heliyon.2024.e33949
25. Iqbal Z, Hakeem AKA, Yashodha S, Al-Mdallal QM, Alhazmi SE, Alqahtani B, Fathima D, Eldin ET. Analysis of entropy generation in the flow of MHD water-ethylene glycol nanofluid over a spinning down pointing vertical cone. Int J Thermofluids. 2023; 20:100447. https://doi.org/10.1016/j.ijft.2023.100447
26. Mishra SR, Panda S, Baithalu R. Enhanced heat transfer rate on the flow of hybrid nanofluid through a rotating vertical cone: a statistical analysis. Partial Differ Equ Appl Math. 2024; 11:100825. https://doi.org/10.1016/j.padiff.2024.100825
27. Manjunatha S, Srilatha P, Santhosh Kumar J, Venkadeshwaran K, Varma SVK, Nagaraja KV, Varshney G. Hydromagnetic convective and radiative heat transfer in Fe3O4-CoFe2O4/H2O flow over a permeable surface. Bionanoscience. 2025; 15(1):101. https://doi.org/10.1007/s12668-024-01692-7
28. Tanuja TN, Kavitha L, Varma SVK, Raju VCC, Kumar GC, Eid MR, Hussain SM. Heat and mass transfer analysis of Casson-based hybrid nanofluid flow in the presence of an aligned magnetic field: an application toward mechanical engineering. Proc Inst Mech Eng Part N J Nanomater Nanoeng Nanosyst. 2024. https://doi.org/10.1177/23977914241248546
29. Karuppasamy M, Saravanan R, Chandrasekaran M, Muthuraman V. Numerical exploration of heat transfer in a heat exchanger tube with cone shape inserts and Al2O3 and CuO nanofluids. Mater Today Proc. 2020; 21:940-7. https://doi.org/10.1016/j.matpr.2019.08.242
30. Manjunatha S, Santhosh Kumar J, Ur Rehman K, Shatanawi W, Varma SVK. Thermal radiation and thermo-diffusion in Casson-ferrofluid over a magnetized porous surface: RSM analysis. Int J Thermofluids. 2025; 26:101130. https://doi.org/10.1016/j.ijft.2025.101130
31. Tanuja TN, Kavitha L, Ur Rehman K, Varma SVK, Shatanawi W, Kumar GV. Parametric analysis for Thermally Magnetized Hybrid Ternary (TMHT) nanofluid flow on thin film with temperature stratification. Int J Thermofluids. 2025; 26:101089. https://doi.org/10.1016/j.ijft.2025.101089
32. Manjunatha S, Ammani Kuttan B, Tanuja TN. Sensitivity analysis of thermal optimisation within the conical gap between the cone and the surface of the disk with particle deposition. J Therm Anal Calorim. 2025; 150(1):361-75. https://doi.org/10.1007/s10973-024-13866-2

Nomenclature

u, v & w	The velocity components in the x, y and z θ directions, respectively. (m/s)	M	Magnetic field
N_1	Velocity slip factor	Fr	Darcy-Forchheimer
D_1	Temperature slip factor	k_f	Thermal conductivity (W/mK)
g	Acceleration due to gravity (m/s^2)	C_b	Specific heat at constant pressure (J/kgK)
B_0	Magnetic field strength (tesla)	**Greek symbols**	
Q	Heat source/sink	μ_f	Dynamic viscosity (Kg/m s)
q_w	Surface heat flux (K)	ρ_f	Densiy
T	Fluid temperature (K)	σ_f	Electrical conductivity (S/m)
$f'(\eta)$	Tangential velocity profile	ν_f	Kinematic viscosity (m^2/s)
$\theta(\eta)$	Temperature profile	σ^*	Stefan-Boltzmann constant (W/m^{2}K^2)
$g(\eta)$	Swirl velocity	γ	Vertex angle
Re	Reynolds number	γ_1	Velocity slip parameter
T_∞	Ambient temperature (K)	γ_2	Thermal slip parameter
Nu	Nusselt number	τ	Shear stress
K	Porous medium	Ω	Angular velocity
Gr	Thermal Grashof number		